SPECIAL FEATURE

Three-Phase Bidirectional EV Charging Infrastructure for G2V & V2G Applications

Silicon University

The Science & Technology Magazine

Digital Digest

Vol. 34 ● April – June 2026

Our Mission: “To provide the best of technical skills, professional ethics and human values in enriching the disciplines of Sciences, Engineering and Technology for Social development and Nation building”.

Adaptive Learning using AI: Rethinking the Industrial Education Model

Education systems worldwide stand at a critical crossroads. For over a century, education has largely followed an industrial model characterized by standardized curricula, uniform pacing, age-based grouping, and assessment systems designed for efficiency rather than individuality. While this approach successfully expanded access to education during the industrial era, it is increasingly misaligned with the demands of a rapidly evolving, knowledge-driven society. The emergence of Artificial Intelligence (AI) is now challenging these traditional frameworks by enabling adaptive learning that personalizes education according to individual learner needs.

Adaptive learning uses AI to tailor educational experiences based on each learner's pace, abilities, prior knowledge, and progress. Unlike the traditional "one-size-fits-all" approach, AI-driven systems continuously analyze student performance in real time, identify learning gaps, recommend appropriate learning resources, and dynamically adjust instructional content and difficulty levels. This transformation extends beyond technological advancement, representing a fundamental shift in how education is designed, delivered, and evaluated.

The industrial model emphasized standardization and predictable outcomes, with all students progressing through the same curriculum at a uniform pace. Although this approach improved access to education, it often overlooked differences in learning styles, abilities, interests, and motivation. As a result, struggling learners frequently fell behind, while advanced learners received insufficient intellectual challenge. These limitations demonstrate the need for a more flexible, personalized, and learner-centered educational framework.

In contrast, adaptive learning places the learner at the centre of the educational process. It enables personalized learning pathways that allow students to revisit difficult concepts, receive immediate feedback, progress according to their own pace, and explore advanced topics when they are ready. By adapting instruction to individual learning needs, AI enhances student engagement, improves conceptual understanding, and strengthens long-term knowledge retention. Moreover, adaptive learning promotes inclusivity by accommodating learners with diverse educational backgrounds, abilities, and learning preferences, thereby creating more equitable learning opportunities.

AI also has the potential to redefine the role of teachers. Rather than functioning primarily as information providers, educators can become facilitators and mentors who support meaningful learning experiences. By automating routine tasks such as grading, performance monitoring, and personalized content recommendations, AI allows teachers to devote more attention to developing students' creativity, critical thinking, collaboration, and problem-solving skills.

However, the transition to AI-driven education also presents significant challenges. Concerns related to data privacy, algorithmic bias, ethical use of student information, and unequal access to digital technologies must be addressed to ensure fair implementation. Excessive dependence on AI may also reduce opportunities for social interaction and collaborative learning. Therefore, a balanced approach that combines AI-powered adaptive learning with human guidance is essential for creating responsive, inclusive, and learner-centred educational environments that prepare students for the demands of the twenty-first century.

Dr. Pragyan Paramita Das
Dept. of CSE

Three-Phase Bidirectional EV Charging Infrastructure for G2V and V2G Applications

***Abstract** – This study presents a high-performance, three-phase grid-connected EV charging system capable of bidirectional power transfer, supporting both Grid-to-Vehicle (G2V), Inductor-Capacitor-Inductor (LCL) and Vehicle-to-Grid (V2G) operations. The system integrates a bidirectional Voltage Source Converter (VSC), an LCL filter, and a battery-side bidirectional DC-DC converter, coordinated through a cascaded control strategy based on Synchronous Reference Frame (SRF) theory and PI controllers. A Phase-Locked Loop (PLL) ensures synchronization with the grid, while the control scheme maintains unity power factor and low Total Harmonic Distortion (THD) in grid currents. Simulations confirm sinusoidal, balanced, in-phase current waveforms in both directions, with DC-link voltage regulated within ±5–6 V. Battery charging/discharging is precisely managed, achieving 94% and 91% efficiency respectively, with SoC maintained within safe limits. These results validate the system's ability to deliver high-quality power exchange, grid stability, and reliable battery control—making it suitable for smart grid applications with high EV penetration.*

***Keywords** — EV, V2G, G2V, Power Quality, PLL, Bidirectional Converter, Battery*

I. Introduction

With rising Electric Vehicle (EV) adoption driven by sustainability goals and CO_2 reduction targets, efficient and intelligent charging infrastructures are increasingly essential [1]. Conventional EV chargers, based on unidirectional power flow, treat vehicles solely as energy consumers and lack interaction with the grid [2][3][4]. To address this, bidirectional charging systems are gaining traction, enabling both Grid-to-Vehicle (G2V) and Vehicle-to-Grid (V2G) operations [5]. As EVs often remain idle with full batteries, they can act as distributed energy resources, supporting the grid during peak demand, improving reliability, and providing financial benefits to owners [6]. The proposed control strategy further compensates for harmonic disturbances from frequent charge/discharge cycles, ensuring voltage and current stability at the Point of Common Coupling (PCC) and reinforcing overall grid reliability [7, 8]. For control, a Synchronous Reference Frame (SRF) approach integrated with a Phase-Locked Loop (PLL) is used to decompose grid currents and regulate active/reactive power. A Proportional-Integral (PI) controller maintains voltage and current stability, while Pulse-Width Modulation (PWM) enhances output waveform quality and minimizes Total Harmonic Distortion (THD). Overall, the system addresses key challenges in modern EV integration by improving power quality at the PCC, supporting reliable grid operation, and offering operational and economic benefits through bidirectional energy exchange.

II. System Description

The proposed system is a three-phase grid-connected Electric Vehicle (EV) charging and discharging station designed to operate in both Grid-to-Vehicle (G2V) and Vehicle-to-Grid (V2G) modes as presented in Fig. 1. The main components and functional blocks of the system are described below:

A. Three-Phase Grid-Connected Configuration

The system is connected to a standard three-phase AC grid, allowing for high-capacity energy transfer. This configuration supports efficient charging of the EV battery during off-peak hours and discharging to the grid during peak load periods. The system interfaces with a balanced three-phase AC grid to facilitate higher power transfer. The grid voltages are given by equation 1:

$$v_a = V_m \sin \omega t \quad v_b = V_m \sin(\omega t - 120^0) \tag{1}$$

where V_m is the peak voltage and ω is the angular frequency of the grid.

B. LCL Filter

An LCL filter is installed between the grid and the Voltage Source Converter (VSC) to attenuate high-frequency switching harmonics. This helps maintain the power quality by reducing Total Harmonic Distortion (THD) at the Point of Common Coupling (PCC). The equivalent impedance of the LCL filter is given by equation 2:

$$Z_{LCL}(S) = L_1 S \frac{1}{C_f S} + L_2 S \tag{2}$$

where:

- L_1 is the converter-side inductor
- L_2 is the grid-side inductor
- C_f is the filter capacitor
- S is the Laplace variable

This filter ensures a reduction in Total Harmonic Distortion (THD) and improves compliance with IEEE 519 standards.

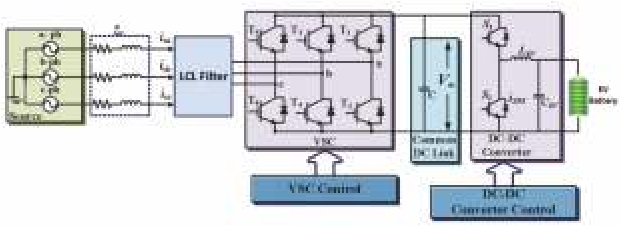

Fig. 1. Block diagram of a three-phase grid-connected EV charging system operating in bidirectional G2V/V2G modes

C. AC-DC Conversion Stage

The AC-DC conversion is carried out using a three-phase bidirectional voltage source converter (VSC), which performs active power conversion from AC to DC during charging (G2V) and from DC to AC during discharging (V2G). This rectifier ensures sinusoidal input currents and regulated DC output voltage. In Grid-to-Vehicle (G2V) mode, the VSC operates as a rectifier, converting three-phase AC power from the grid into regulated DC power to charge the EV battery. In Vehicle-to-Grid (V2G) mode, it functions as an inverter, converting DC power from the EV battery back into synchronized AC power that is injected into the grid. The average DC output voltage of the Voltage Source Converter (VSC) (under ideal conditions) is given by equation 3:

$$V_{dc} = \frac{3\sqrt{2}}{\pi} V_{LL} \tag{3}$$

Where V_{LL} is the RMS value of the AC line-to-line voltage.

In controlled rectifier mode (using VSC and PWM), this becomes equation 4:

$$V_{dc} = mV_m \tag{4}$$

Where, m is the Modulation index ($0 < m < 1$), V_m is the peak value of the input voltage (v).

In V2G mode, the inverter must synchronize with the grid. This is achieved via a Phase-Locked Loop (PLL), ensuring proper frequency and phase matching.

D. DC-DC Battery Charging/Discharging Converter

A bidirectional DC-DC converter connects the DC link of the VSC to the EV battery. It regulates the charging and discharging current based on the system mode and battery state-of-charge (SoC). The duty cycle (D) of this converter is dynamically controlled to manage energy flow and protect the battery. For a non-isolated bidirectional buck-boost converter output voltage is given in equation 5 and 6:

$$V_{dc} = \frac{V_{bat}}{1-D} \tag{5}$$

In buck (G2V) mode:

$$V_{dc} = DV_{bat} \tag{6}$$

where:

- V_{DC} is the DC link voltage
- V_{bat} is the battery terminal voltage
- D is the duty cycle.

E. EV Battery

The system is interfaced with a high-capacity lithium-ion battery typically used in electric vehicles. This battery acts as an energy sink during G2V mode and as an energy source during V2G operation. The battery dynamics are simplified as equation 7:

$$P_{bat} = V_{bat} I_{bat} \tag{7}$$

Where :

- P_{bat} is the battery power (positive during discharge, negative during charge)
- V_{bat} and I_{bat} are the battery voltage and current respectively

III. Control Scheme

The control system is built upon Synchronous Reference Frame (SRF) theory, Phase-Locked Loop (PLL) synchronization, and Proportional-Integral (PI) controllers to ensure accurate and stable bidirectional power flow between the grid and the electric vehicle (EV).

A. Grid-Side VSC Control

The VSC regulates the power flow between the grid and the EV battery by implementing vector control in the SRF (dq frame). The control structure includes a cascaded system comprising an outer DC-link voltage control loop and an inner current control loop. The system also employs an SRF-PLL for synchronization with the grid.

- *Synchronous Reference Frame (SRF) transformations*

The grid currents are transformed from the stationary *abc*-frame to the rotating *dq*-frame using Park's transformation. Here, the current I_d controls the active power and and I_q controls the reactive power.

- *Phase-Locked Loop (PLL):*

The SRF-PLL is used to estimate the grid phase angle θ and frequency ω, enabling precise *dq* transformations and synchronization. The q-axis component of the grid voltage is regulated to zero to maintain phase alignment as in equation 8, 9 and 10:

$$v_q = V_m sin(\emptyset - \theta) \tag{8}$$

The PLL is implemented using a PI controller:

$$\omega = \omega_{nom} + K_{p\_PLL} v_q + K_i \int v_{q\_PLL} dt \tag{9}$$

$$\theta(t) = \int \omega dt \tag{10}$$

This ensures that the θ tracks the grid angles.

- DC-Link Voltage Control

The DC link connects the grid-side VSC and the battery-side DC-DC converter. Its voltage must be tightly controlled to ensure bidirectional power flow stability. The DC link serves as a buffer between grid and battery-side power exchange. Also, it ensures the dynamic response during mode switching (G2V ↔ V2G).

The DC link voltage controller ensures stable DC voltage. Control is applied on the d-axis current i_d, which controls real power. Use the DC-link voltage error as in equation 11, to generate a reference i_d^*.

$$V_{dc\_err} = V_{dc\_ref} - V_{dc} \tag{11}$$

$$i_d^* = K_{p\_DC} V_{dc\_err} + K_{i\_DC} \int V_{dc\_err} dt \tag{12}$$

This i_d^* becomes the input for the inner current controller

- *Inner Current Control Loop:*

The inner-loop PI controllers regulate the d-axis and q-axis currents are given by equation 13-16.

$$E_d = K_{p\_d} \left(I_{d\_ref} - I_d\right) + K_{i\_d} \int \left(I_{d\_ref} - I_d\right) dt \tag{13}$$

$$E_q = K_{p\_q} \left(I_{q\_ref} - I_q\right) + K_{i\_q} \int \left(I_{q\_ref} - I_q\right) dt \tag{14}$$

The control voltages in the dq frame are:

$$U_d = \frac{2}{V_{DC}} (E_d + V_d + L\omega I_q) \tag{15}$$

$$U_q = \frac{2}{V_{DC}} (E_q + V_q + L\omega I_d) \tag{16}$$

These are converted back to the stationary frame through the inverse Park transformation as given by equation 17:

$$[U_\alpha \; U_\beta] = \begin{bmatrix} cos\,cos\,\theta & -sin\,sin\,\theta \\ sin\,sin\,\theta & -cos\,cos\,\theta \end{bmatrix} [U_d \; U_q] \tag{17}$$

Finally, the three-phase voltage references are derived as given by equation 18:

$$[V_{a\_ref} \; V_{b\_ref} \; V_{c\_ref}] = \sqrt{\frac{2}{3}} \left[1\,0 - \frac{1}{2}\sqrt{\frac{3}{2}} - \frac{1}{2} - \sqrt{\frac{3}{2}}\right] [U_\alpha \; U_\beta] \tag{18}$$

- *Pulse Width Modulation (PWM):*

The reference voltages are used to generate modulation signals as given by equation 19:

$$m_n = \frac{2V_{n\_ref}}{V_{DC}};\; n = a, b, c \tag{19}$$

Accordingly, the switching pulses are determined a as given by equation 20:

$$S_x = \{1,\; if\; m_x > carrier\; 0,\; otherwise;\; x = 1 - 6 \tag{20}$$

B. Battery-Side Converter Control

The battery-side bidirectional DC-DC converter plays a critical role in regulating the charging and discharging current of the EV battery. It ensures bidirectional energy flow, operating in buck mode during Grid-to-Vehicle (G2V) charging and in boost mode during Vehicle-to-Grid (V2G) discharging. The converter is governed by a closed-loop feedback control mechanism designed to maintain battery current and voltage within safe operational limits, enhancing system efficiency and battery lifespan. The control architecture is based on Pulse-Width Modulation (PWM) switching and Proportional-Integral (PI) control strategies. Additionally, the operating mode (G2V or V2G) is selected dynamically based on system-level parameters such as the SoC and grid demand conditions.

- *G2V Mode (Charging):*

In charging mode, the converter operates in buck mode, stepping down the DC-link voltage, V_{DC} to to match the battery voltage, V_{bat}. The control objective in this mode is to regulate the charging current to a desired reference level, I_{bat_ref}, ensuring smooth and safe energy transfer. A PI controller is used to compute the duty cycle (D_{buck}) for the PWM switch based on the error between the reference and actual battery current as given by equation 21 and 22:

$$I_{bat\_err} = I_{bat\_ref} - I_{bat} \tag{21}$$

$$D_{buck} = K_{p\_bat} I_{bat\_err} + K_{i\_bat} \int I_{bat\_err}\, dt \tag{22}$$

- *V2G Mode (Discharging):*

In discharging mode, the converter functions as a boost converter, stepping up the battery voltage, V_{bat} to the dc-link voltage, V_{DC} . The control objective can either be to maintain a constant DC-link voltage or to regulate the discharging current into the grid. A PI controller is used to generate the required duty cycle (D_{boost}) by minimizing the error between the reference and measured DC-link voltage:

$$V_{DC\_err} = V_{DC\_ref} - V_{DC} \tag{23}$$

$$D_{boost} = K_{p\_DC} V_{DC\_err} + K_{i\_DC} \int V_{DC\_err}\, dt \tag{24}$$

Table – I summarizes the multiple cascaded control loops employed in the proposed EV charging /discharging system. Each loop performs a distinct function that collectively ensures system stability, grid synchronization, power quality improvement, and battery protection. The inner-outer loop architecture provides fast dynamic response while maintaining precise regulation of power and voltage variables in both Grid-to-Vehicle (G2V) and Vehicle-to-Grid (V2G) modes.

Table -1: Description of Control Loops, Regulated Variables, and Controller Roles in G2V/V2G Operation

Control Loop	Variable Regulated	Controller Type	Role
SRF-PLL	θ (phase), ω (frequency)	PI	Synchronizes converter control with grid voltage phase and frequency
DC-link Voltage Control	V_{dc}	PI	Outer loop regulating real power flow by generating, i_d^*
Current Control Loop	i_d, i_q	PI	Inner loop controlling active (P) and reactive (Q) power components
Battery Current Control	I_{bat}	PI	Regulates charging/discharging current for battery safety and SoC management

IV. Result Analysis

The performance of the proposed grid-interfaced bidirectional EV off-board charger was analyzed under both Grid-to-Vehicle (G2V) and Vehicle-to-Grid (V2G) operating conditions. The system was simulated using a 400 V (L-L), 50 Hz three-phase grid connected to a 400 V, 32 Ah lithium-ion battery via a bidirectional voltage source converter (VSC). Control strategies based on Synchronous Reference Frame (SRF) theory with Proportional-Integral (PI) regulators were employed to improve power quality, ensure grid compliance, and maintain system stability.

A. Grid Performance During G2V/V2G Operation

During G2V operation, the three-phase grid voltages (V_A, V_B, V_C) remained sinusoidal and balanced at the rated RMS value of 400 V. As shown in Fig. 2 (a), the voltage waveforms were distortion-free and maintained correct 120° phase separation. However, in the absence of control, the corresponding grid currents (I_A, I_B, I_C) were highly distorted due to the nonlinear nature of the charger's input rectification stage, exhibiting a Total Harmonic Distortion (THD) of approximately 12.6%, thereby degrading the power quality.

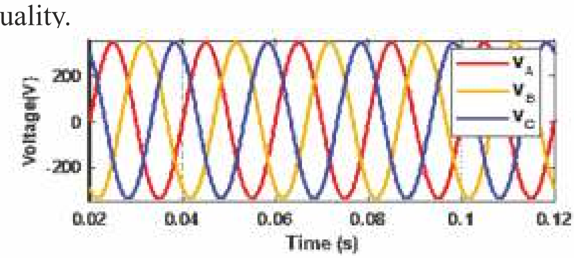

(a)

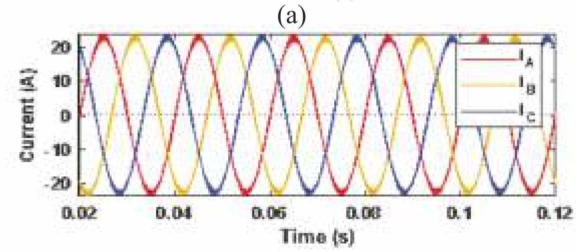

(b)

Fig. 2.(a) Grid voltage - G2V/V2G mode (b) Grid current – G2V mode

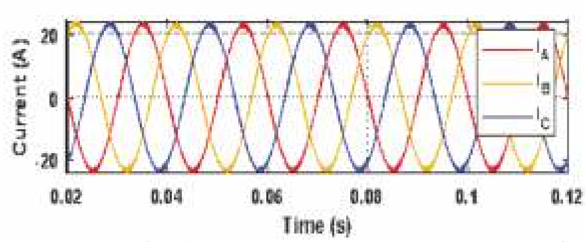

Fig. 3.Grid Voltage & Current During - V2G Mode

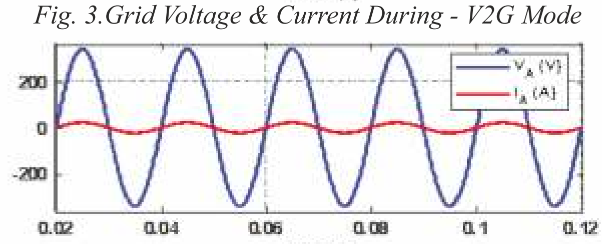

(a)

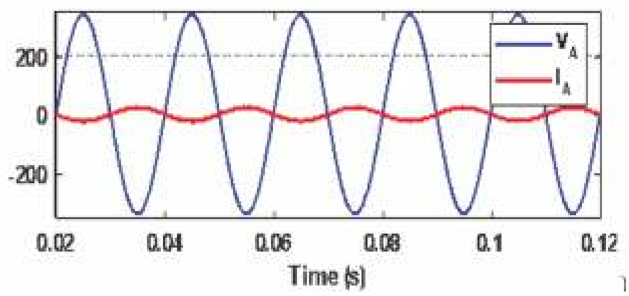

(b)

Fig. 4. 1-ph Grid Voltage & Current During – (a) G2V (b) V2G Mode

The grid currents became sinusoidal, balanced, and in-phase with their respective voltages, as depicted in Fig. 2 (b). This resulted in a near-unity power factor of 0.99, indicating effective harmonic mitigation and phase alignment. The THD was substantially reduced from 12.6% to 2.4%, thus ensuring compliance with IEEE 519 harmonic standards. As shown in Fig. 3, the corresponding grid currents (I_A, I_B, I_C) reverse polarity—reflecting the change in power direction—but continue to exhibit a sinusoidal shape and remain in-phase with their respective voltage waveforms. A closer examination of Phase A behavior further reinforces this observation: as illustrated in Fig. 4 (a) for G2V mode, the current waveform is positive and in-phase with the voltage, indicating active power draw. In contrast, during V2G, as shown in Fig. 4 (b), the current waveform becomes negative yet remains in-phase, signifying active power injection back into the grid.

B. Battery Performance and SoC Analysis

The battery parameters were continuously monitored throughout the bidirectional operation to ensure system safety, performance efficiency, and battery health. During G2V operation, the battery current was positive and regulated at a constant value of approximately 30 A during the initial constant current (CC) phase. As the battery voltage approached its maximum threshold of 387.1 V, the system transitioned to constant voltage (CV) regulation, leading to a gradual tapering of current, ensuring safe and efficient charging. The battery voltage increased smoothly from approximately 360 V to 387 V, corresponding to a SoC increase from 51.6441% to 51.6444%, over a period of 0.5s, as shown in Fig. 5 (a). The current profile, depicted in Fig. 5 (b), remained steady during the CC stage and gradually declined during CV regulation. The charging efficiency was calculated to be approximately 94%, based on energy measured at the DC bus.

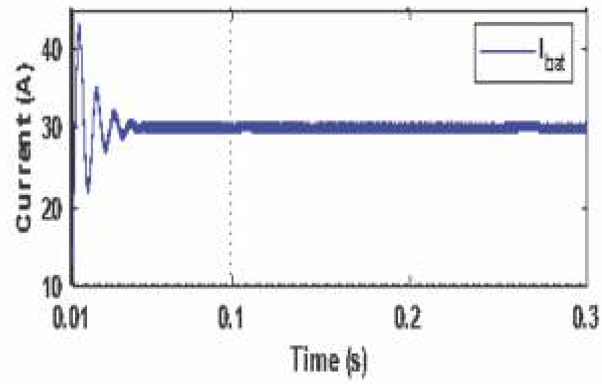

(a)

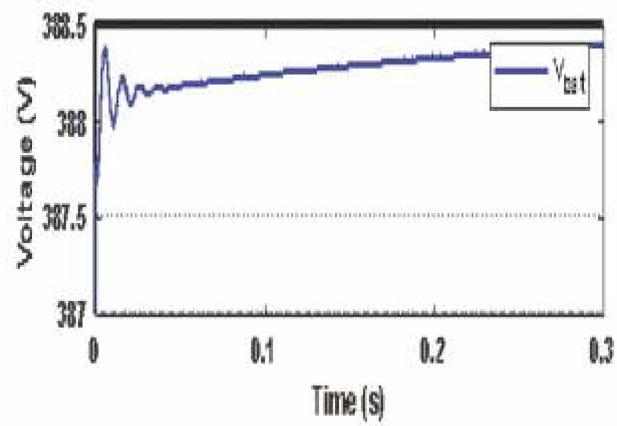

(b)

Fig. 5.(a) Battery Voltage & (b) Current – G2V Mode

In V2G mode, the battery current reversed polarity, becoming negative, indicating energy being supplied back to the grid. The current was controlled within the range of −29 A to −30 A, ensuring smooth and stable discharge. The battery voltage decreased from 400 V to approximately 388.5 V, as the SoC dropped from 51.644% to 51.641% over a 0.5s interval, as shown in Figs. 6 (a) and 6 (b) for voltage and current, respectively. The discharge efficiency was observed to be around 91%.

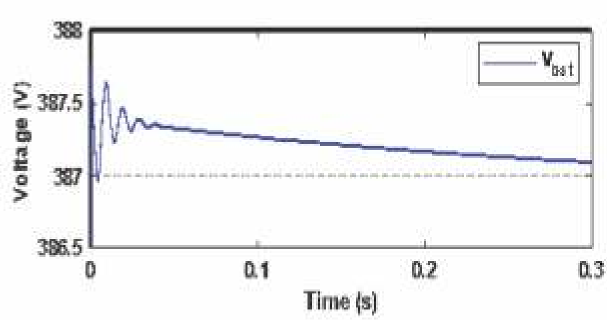

(a)

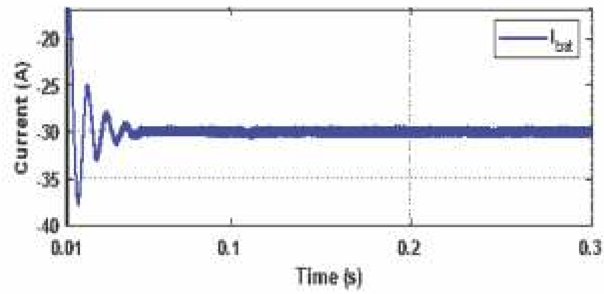

(b)

Fig. 6.(a) Battery Voltage & (b) Current – V2G Mode

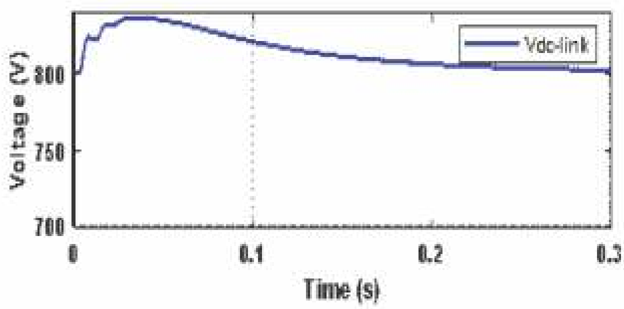

(a)

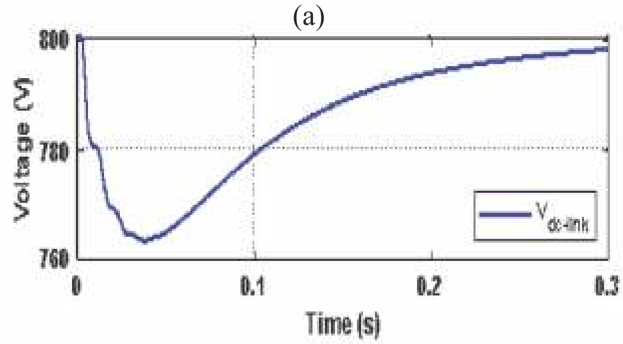

(b)

Fig. 7. DC-link Voltage (a) G2V & (b) V2G Mode

Overall, the system demonstrates high efficiency, safe operation, and effective SoC management under both charging and discharging conditions. These performance metrics validate the suitability of the proposed bidirectional charging system for real-world Vehicle-to-Grid (V2G) applications and sustainable energy integration.

C. DC-Link Voltage Regulation and Stability

The DC-link voltage, acting as a critical energy buffer between the AC and DC stages, was thoroughly evaluated as a key indicator of system stability and dynamic performance. In the absence of control, the DC-link voltage exhibited significant ripple—up to ±30 V—which could compromise the efficiency, converter reliability, and battery safety, while also increasing stress on the power electronics components.

However, with the implementation of the proposed control strategy, the DC-link voltage was tightly regulated around the nominal value of 400 V, with minimal voltage ripple observed under both operating modes. Specifically, during Grid-to-Vehicle (G2V) operation, the voltage ripple was reduced to approximately ±36 V, while during Vehicle-to-Grid (V2G) mode, it remained within ±37 V, as illustrated in Fig. 7 (a) and Fig. 7 (b), respectively.

Table–2: Summary of System Performance in G2V/V2G Modes

Parameter	G2V Mode	V2G Mode
Grid Voltage (RMS)	400 V (Line-to-Line)	400 V (Line-to-Line)
Grid Current	Sinusoidal, in-phase	Sinusoidal, reversed polarity
Grid Current THD (%)	2.4	2.5
Power Factor	~0.99	~0.99
Battery Voltage Range	360–415 V	415–370 V
Battery Current	+20 A (charging)	−18 A (discharging)
Battery SoC Change	40% → 90%	90% → 30%
DC-Link Voltage Ripple	±5 V	±6 V
Charging Efficiency	94%	—
Discharging Efficiency	—	91%
Reactive Power Support	Yes	Yes

The waveforms in Fig. 2 – Fig. 7 demonstrate the system's grid compatibility, power quality, and efficiency under various conditions. As summarized in Table II, the SRF-based control notably improved grid current quality, battery regulation, and DC-link voltage stability.

V. Conclusions

This work presents a three-phase grid-connected EV charging system capable of bidirectional G2V and V2G operation. The system integrates an LCL filter, a bidirectional VSC, and a DC-DC converter, controlled through a cascaded PI-based scheme in the Synchronous Reference Frame (SRF). Simulation results confirmed stable DC-link voltage, efficient battery control, and high-power conversion efficiency—94% during charging and 91% during discharging. The system maintained sinusoidal grid currents with low harmonic distortion in compliance with IEEE-519 standards and operated at near-unity power factor. Overall, the proposed system enables reliable and efficient bidirectional power flow while preserving grid stability and power quality, making it well-suited for smart grid integration and clean energy applications.

References

[1] International Energy Agency (IEA), Global EV Outlook 2023: Catching up with climate ambitions, Paris: IEA, 2023. [Online]. Available: https://www.iea.org/reports/global-ev-outlook-2023

[2] A. Emadi, Y. J. Lee, and K. Rajashekara, "Power electronics and motor drives in electric, hybrid electric, and plug-in hybrid electric vehicles," IEEE Transactions on Industrial Electronics, vol. 55, no. 6, pp. 2237–2245, Jun. 2008.

[3] T. Jiang, J. Zhang, X. Wu, K. Sheng and Y. Wang, "A Bidirectional LLC Resonant Converter With Automatic Forward and Backward Mode Transition," in IEEE Transactions on Power Electronics, vol. 30, no. 2, pp. 757-770, Feb. 2015.

[4] A. Golder and S. S. Williamson, "Energy Management Systems for Electric Vehicle Charging Stations: A Review," IECON 2022 – 48th Annual Conference of the IEEE Industrial Electronics Society, Brussels, Belgium, 2022, pp. 1-6

[5] F. Blaabjerg, Y. Yang, K. A. Kim and J. Rodriguez, "Power Electronics Technology for Large-Scale Renewable Energy Generation," in Proceedings of the IEEE, vol. 111, no. 4, pp. 335-355, April 2023.

[6] Willett Kempton, Jasna Tomić, Vehicle-to-grid power fundamentals: Calculating capacity and net revenue, Journal of Power Sources, Volume 144, Issue 1, 2005, Pages 268-279.

[7] Sithara S.G. Acharige, Md Enamul Haque, Mohammad Taufiqul Arif, Nasser Hosseinzadeh, Kazi N. Hasan, M.J. Hossain, Kashem M. Muttaqi, Grid integration of electric vehicles - Impact assessment and remedial measures, Journal of Power Sources, Volume 650, 2025, 236697.

[8] F. Blaabjerg, M. Liserre and K. Ma, "Power Electronics Converters for Wind Turbine Systems," in IEEE Transactions on Industry Applications, vol. 48, no. 2, pp. 708-719, March-April 2012.

Ashutosh Patra, Rakesh Kumar Bariki,
Shubhranshu Das, Arpita Samal, Kajol Behera
Dept. of EEE

Battery-Free Artificial Photosynthesis Turns Sunlight, Water, and CO_2 into Fuel

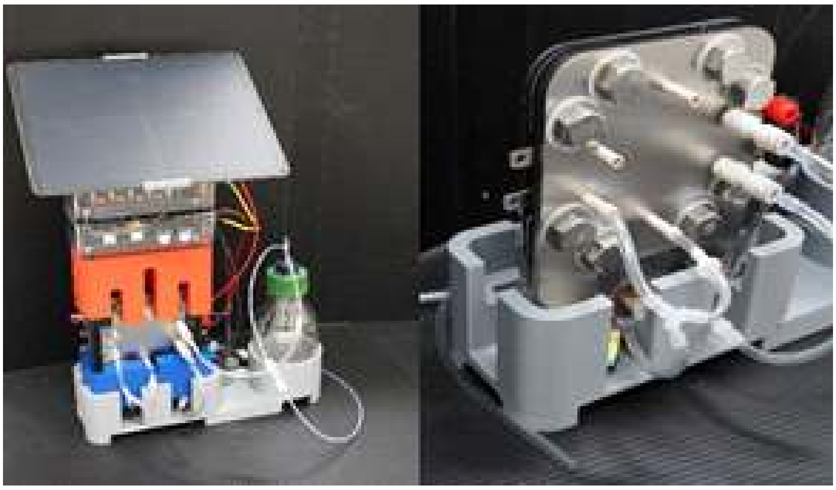

Researchers at Osaka Metropolitan University have created a new artificial photosynthesis system that can produce solar fuel more consistently while eliminating the need for battery-based control systems. The advance comes from incorporating a self-regulating chemical component directly into the electrolyzer, and removing one of the more costly elements commonly used in these technologies. Like natural photosynthesis in plants, artificial photosynthesis uses sunlight to transform water and carbon dioxide into useful fuels. One example is formic acid, a chemical that can store energy for later use. To simplify the system, a research team led by Associate Professor Yasuo Matsubara and Professor Yutaka Amao at the Research Center for Artificial Photosynthesis at Osaka Metropolitan University, working with Iida Group Holdings Co., Ltd, redesigned the electrolyzer using a special solid electrolyte. In the new design, the electrolyzer performs the Maximum Power Point Tracking (MPPT) function on its own, removing the need for batteries and external control hardware. Rather than relying on separate electronics, converters, and batteries to optimize performance, the electrolyzer automatically adjusts its electrical characteristics by varying its thermal and impedance properties.

Source: https://scitechdaily.com/

Humanoid Robots Race

The world's first humanoid robot half-marathon was held on April 19, 2025, in Beijing, where robots and humans competed side by side on the same course. A total of 20–21 humanoid robots, along with more than 12,000 amateur runners, joined the event. Only six robots managed to finish the 21.0975 km course, though many completed the race smoothly and some even outpaced professional athletes. The champion robot recorded a time of 2 hours 40 minutes, comfortably ahead of its machine rivals but more than double the time of the human winner in the conventional race.

Source: The Indian Express

Claude AI Automation Tools

The AI startup Anthropic launched Claude for Small Business in May 2026. This is a tailored offering that integrates with everyday business tools to help small firms automate payroll, invoices, marketing, and customer service tasks. Claude is Anthropic's family of AI models, named after Claude Shannon, the father of information theory. It can be used to automate tasks such as invoice tracking, meeting summaries, marketing content creation, document organisation, and customer communication. It can also handle natural language conversation, writing and editing text, coding and debugging, analyzing documents, spreadsheets, and data, as well as automating workflows across tools like Google Workspace, Microsoft 365, Slack, QuickBooks, and PayPal.

Source: The Indian Express

Semiconductor Fabrication Plant

India's first front-end semiconductor fabrication plant, aimed at accelerating efforts to build a domestic chip industry, is being developed by Tata Electronics and ASML in Dholera, Gujarat. The facility is designed to produce chips for applications ranging from automotive and mobile devices to artificial intelligence, backed by an investment of $11 billion. The Dutch chipmaking equipment maker's technology will support Tata Electronics' planned 300-millimetre semiconductor fabrication plant in Gujarat.

Source: The Indian Express

3D Computing Device

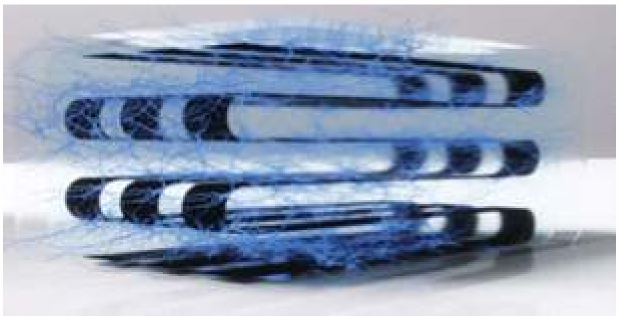

Researchers from Princeton University have invented a three-dimensional device that combines real biological neurons with advanced electronics in a single working system. Previous attempts to use brain cells for computation faced limitations because the neurons and electronic components were not fully integrated. Using advanced fabrication techniques, the team built a three-dimensional scaffold of tiny metal wires and electrodes, coated with a soft, flexible material designed to support living neurons. This structure allowed tens of thousands of neurons to grow into and around the electronic network, forming a biological neural system tightly integrated with electronics. The device can both record signals from the cells and stimulate them, creating a dynamic feedback loop. It can also be programmed using computational methods to identify and recognize patterns. So far, the system has been able to recognize relatively simple patterns under controlled conditions. The researchers hope to refine the platform so that, in the future, it can handle more complex tasks — potentially opening the door to new forms of biohybrid computing that blend biology and technology in powerful ways.

Source: The Indian Express

Flaw in AI Symptom Checkers

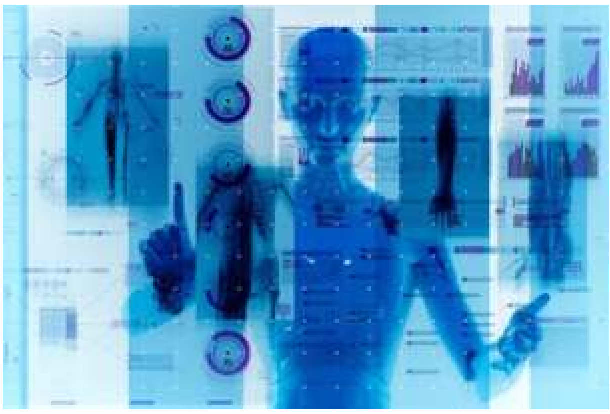

Before visiting a doctor in the future, patients may first answer questions from an AI system. Based on those responses, the AI could decide whether the condition is urgent or when an appointment should be scheduled. But researchers found that distrust in AI makes people give less detailed symptom reports, which reduces the accuracy of these digital assessments. In a study with 500 participants, people were asked to describe symptoms of headaches and flu-like conditions. Some were told their reports would be reviewed by a human doctor, while others believed an AI chatbot would read them. The difference was clear: reports written for doctors were longer and more detailed than those written for chatbots. This shows that when patients don't trust a machine to understand their uniqueness, they unconsciously withhold important details. As a result, even advanced AI systems may struggle to provide precise assistance. Researchers concluded that improving technology alone won't solve the problem. Better user interface design and stronger communication between patients and digital systems will be essential to make AI healthcare tools more effective.

Source: Scitech Daily

Photon-driven Nano Robots

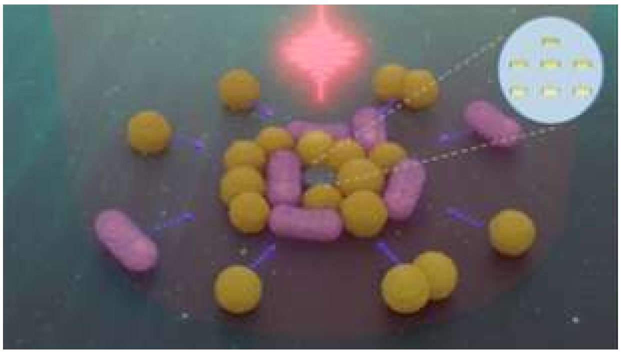

Tiny robots, about 50 times smaller than the width of a human hair, are opening new possibilities for working at microscopic scales. They allow scientists to manipulate objects far beyond the reach of human hands, moving closer to the long-standing goal of directly interacting with single cells and bacteria in liquid environments. One of the biggest hurdles has been figuring out how to power and steer machines at such a tiny scale. The breakthrough comes from plasmonic nanoantennas built into the devices. These antennas absorb light and re-emit it in a controlled direction. Each emitted photon creates a tiny push — like the recoil from firing a bullet — giving the robots both energy and guidance. This light-driven design makes the nanorobots highly agile. They can perform sharp 90° turns, scan large sample areas efficiently, and selectively capture, transport, and release bacteria. For the first time, tasks like collecting and relocating microorganisms can be done with precision, opening new doors for biological research and medical applications. By combining speed, control, and adaptability, these nanorobots demonstrate how scientists are beginning to bridge the gap between technology and the microscopic world.

Source: Scitech Daily

Dr. Chittaranjan Mohapatra
Dept. of CSE

ML-Aided Moderation System to Detect Offensive Comments Posted in the Social Media Platforms

Abstract *– The rapid growth of social media has led to a significant increase in online hostilities, including hurtful behaviour, abusive language, and offensive comments. Studying the historical data over five years, the consequences of this on young vulnerable users has been devastating resulting in depressions, erratic behaviours and even suicides. Our research work presents a precise comparison of results obtained from key Machine Learning (ML) & Deep Learning (DL) models for binary classification of social media comments into two categories, i.e. Offensive or Non-offensive, using benchmark Tweets Dataset available at Kaggle ML repository. We have addressed the class imbalance problem in the dataset by applying four below class imbalance handling techniques. Random Oversampling, Random Under sampling, Class Weight & Synthetic Minority Over-sampling Technique (SMOTE) on Bidirectional Encoder Representations from Transformers (BERT) Embeddings. The fine-tuned Hate BERT model achieved the highest accuracy, confirming its superiority compared to other models. The performance produced by the experiments conducted was done by comparing outcomes received from Logistic Regression, Random Forest, Support Vector Machine (SVM), XGBoost, and Naïve Bayes on Term Frequency-Inverse Document Frequency (TF-IDF).*

Keywords *— TF-IDF, LSTM, HateBERT, SMOTE, NLP*

I. Introduction

Social media platforms such as Twitter, Reddit, Facebook, and YouTube have completely changed the way people communicate and share information online. While these platforms provide great opportunities for connection and expression, they have also become spaces where harmful behavior takes place. One of the most common forms of such behaviour is the posting of offensive comments, where individual deliberately write abusive or harassing content to disturb others and cause emotional harm.

The effects of offensive comments are serious. Victims often suffer from anxiety, depression, and in extreme cases, social withdrawal or self-harm. Young adults and students are especially vulnerable, as they are the most active social media users. The World Health Organization (WHO) has highlighted that negative online experiences are strongly linked to reduced mental well-being, especially among young people.

The massive volume of comments posted on social media every hour makes manual review and moderation practically impossible. Twitter alone sees around 500 million posts per day, making automated detection systems a practical necessity. Early automated systems used simple keyword filtering, which failed to understand context and were easily bypassed. Machine learning improved this significantly, but real-world datasets suffer from class imbalance, where offensive samples are far fewer than non-offensive samples, causing models to perform poorly on the minority class.

This paper presents an ML-aided moderation system that covers the complete pipeline from data collection and preprocessing to training traditional ML models, deep learning models, and the transformer-based HateBERT model, with systematic evaluation of four class imbalance handling techniques.

The objectives of this research are to develop an automated framework for detecting offensive and harmful comments posted on social media platforms through machine learning and deep learning approaches, to collect, preprocess, and explore the dataset, and to establish baseline performance using traditional machine learning and deep learning models. This study aims to evaluate four class imbalance handling techniques — Random Oversampling, Random Under sampling, Class Weight Assignment, and Synthetic Minority Oversampling Technique (SMOTE) — to effectively address data skewness inherent in offensive comment detection tasks. The research further seeks to apply natural language processing techniques for robust text preprocessing and feature representation tailored to social media content. Additionally, this work aims to fine-tune HateBERT, a domain-adapted transformer model, and extract BERT embeddings for downstream classifiers, enabling rich semantic understanding of offensive language. Finally, the research conducts a comprehensive comparative performance analysis of all implemented approaches to identify the best-performing model suitable for real-world deployment in automated content moderation systems.

II. Literature Review

In recent years, automated detection of abusive language, hate speech, and offensive comments using NLP and machine learning techniques has become an important area of research. Several studies have explored classification methods using traditional and deep learning approaches.

Sadiq et al. [1] proposed a deep neural network-based framework for aggression detection on Twitter using the Cyber-Troll dataset of 20,001 tweets, the same dataset used in this work. Their approach combined TF-IDF feature extraction with a bi-gram.

Multilayer Perceptron (MLP), achieving 92% accuracy and 90% F1-score, outperforming CNN-LSTM and CNN-BiLSTM baselines.

Davidson et al. [2] addressed the challenge of distinguishing hate speech from offensive language using approximately 24,802 crowd-sourced tweets. A logistic regression model with TF-IDF weighted n-grams achieved an overall F1-score of 0.90. However, the hate speech class showed lower precision and recall, highlighting the difficulty of minority class detection.

Khanday et al. [3] investigated hate speech detection using COVID-19 Twitter data with a hybrid feature strategy combining TF-IDF and Bag of Words. Stochastic Gradient Boosting achieved 99% precision, 97% recall, and 98% F1-score, demonstrating that hybrid feature representations substantially improve accuracy.

Mac Dermott et al. [4] explored toxic content detection using the Jigsaw dataset with over 223,000 comments. Bidirectional LSTM with Glove embeddings achieved the best performance with an F1-score of 0.922, supporting the use of LSTM and transformer-based models for this task.

The reviewed literature reveals that existing studies either focus on traditional machine learning or deep learning approaches in isolation, without comprehensive side-by-side comparisons under a unified framework. Class imbalance is rarely addressed systematically, and integration of domain-specific trans-former models such as HateBERT in Caselli et al. [5] with SMOTE has not been thoroughly investigated. This work directly addresses all these gaps.

III. Methodology

The proposed method follows a structured five-phase pipeline that progressively addresses text representation, class imbalance, and model capability as shown in Fig 1.

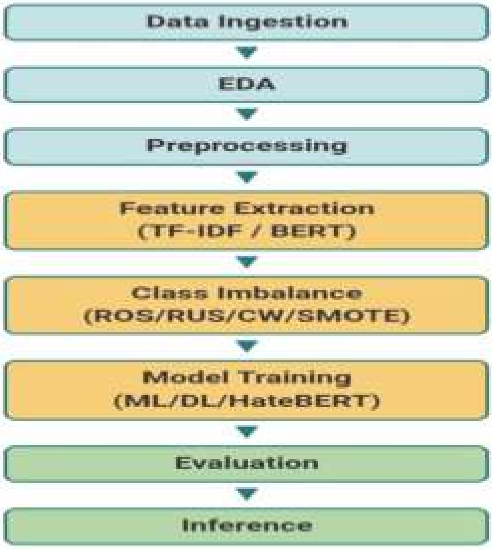

Fig 1. Process Flow Diagram

A. Dataset Description

The dataset used is the publicly available Tweets Dataset for Detection of Offensive Comments, manually crafted by Abhishek Narayanan for a Kaggle NLP challenge focused on detecting the cyber-trolls [2],[6]. The dataset categorizes social media comments into two classes: 1 (Cyber-Aggressive /Offensive) and 0 (Non Cyber-Aggressive /Non-Offensive). It is a JSON-formatted collection of annotated tweets and online comments designed for offensive language and cyber-troll detection tasks. Table 1 illustrates a sample of the first five records from the dataset.

Upon initial loading, the dataset contained 20,001 records with 5,361 duplicate entries. After duplicate removal, 14,640 clean records remained, exhibiting a class imbalance of approximately 80.8% non-offensive and 19.2% offensive samples. The dataset was split into training (70%), validation (15%), and test (15%) subsets using stratified sampling to maintain class distribution across all splits.

Table-1. Sample Dataset Consisting of 5 Offensive Instances

Id	Content	Label
0	Get f**king real dude.	1
1	She is as dirty as they come and that crook...	1
2	Why did you f**k it up. I could do it all day...	1
3	Dude they don't finish enclosing the f**king..	1
4	WTF are you talking about Men? No men...	1

B. Data Preprocessing

Raw social media text is highly noisy and requires thorough cleaning before model training. The following preprocessing steps were applied: conversion to lowercase, URL replacement with a placeholder token, whitespace normalisation, contraction expansion (e.g., "don't" → "do not"), word lemmatisation using NLTK's WordNet Lemmatizer, and removal of rows with non-alphabetic or excessively short content.

C. Feature Extraction

Three feature extraction strategies were implemented. For traditional ML models and ANN, TF-IDF vectorisation was used with 20,000 maximum features, unigram and bigram (1,2) range, sublinear TF scaling, and a minimum document frequency of 2. For RNN and LSTM models, word-level tokenisation was used with a vocabulary of 20,000 tokens and sequences padded to a maximum length of 200 tokens. For HateBERT-based models, the AutoTokenizer associated with GroNLP/hateBERT was used with a maximum sequence length of 128 tokens.

D. Class Imbalance Handling

Random Oversampling (ROS): Minority class samples are duplicated until both classes are equally represented. Simple to implement but may cause overfit-ting on repeated samples.

Random Under sampling (RUS): Majority class sam-ples are randomly removed to equalise class counts. Reduces training data size and may cause underfit-ting for deep learning models.

Class Weight Assignment: The loss function penalises misclassification of minority class samples more heavily using sklearn's compute_class_weight with the balanced setting. The model trains on the com-plete dataset without modifying data distribution.

SMOTE on BERT Embeddings: Dense 768-dimensional contextual embeddings extracted from the fine-tuned HateBERT model are fed into SMOTE, which generates synthetic minority samples by interpolat-ing in the embedding space. This combines the se-mantic richness of transformer representations with SMOTE's balancing capability.

E. Model Architectures

Nine models were implemented and evaluated. Traditional ML models — Logistic Regression, SVM (Linear SVC), Random Forest, XGBoost, and Naïve Bayes — were trained on TF-IDF features with Grid Search CV hyperparameter tuning using 5-fold cross-validation. Deep learning models include an ANN with multiple dense layers and dropout regularisation on dense TF-IDF features, a Simple RNN with an Embedding layer and a recurrent layer of 128 units, and a two-layer stacked LSTM with gating mechanisms to capture long-range dependencies. HateBERT (GroNLP / hateBERT) is a BERT-based model pre-trained on hateful Reddit comments, fine-tuned on the project dataset for 5 epochs using Adam optimiser with class-weighted cross-entropy loss. After fine-tuning, HateBERT was also used as a feature extractor to supply 768-dimensional embed-dings to downstream classifiers.

IV. Simulation Results and Discussions

All models are evaluated using Accuracy, Precision, Recall, F1-score (per class), Macro F1-score, and Confusion Matrices. Macro F1 is the primary evaluation metric, as it equally weights performance across both classes regardless of frequency, providing an unbiased measure for imbalanced classification.

A. Experimental Setup

All experiments were conducted in Google Colab using Python 3.10 with an NVIDIA T4 GPU. Libraries used include scikit-learn 1.3, TensorFlow 2.13, PyTorch 2.0, Transformers 4.35, imbalanced-learn-0.11, and XGBoost 1.7. Random seeds were set to 42 for reproducibility. All deep learning models used

EarlyStopping (patience=5) and ReduceLROnPlateau callbacks.

B. Baseline Results (Without Class Imbalance Handling)

Traditional ML models trained on TF-IDF features without imbalance handling revealed a critical pattern: while macro F1 scores were substantially lower (0.53–0.62), with offensive class recall as low as 10–36%, average performance (10-37%) which is shown in Table-2.

Table – 2. Baseline Model Performance without Imbalance Handling

Model	Macro F1	Class 1 F1	Class 1 Recall
Logistic Regression	0.62	0.35	0.28
SVM (Linear SVC)	0.61	0.37	0.36
XGBoost	0.59	0.28	0.19
Random Forest	0.53	0.17	0.10
Naïve Bayes	0.53	0.17	0.10
ANN (TF-IDF)	0.45	0.00	0.00
Simple RNN	0.45	0.014	0.007
LSTM	0.50	0.10	0.055

Deep learning baseline results were even worse, with the ANN predicting zero offensive samples (Class 1 F1 = 0.00) and the RNN detecting less than 1% of offensive samples. This confirmed that class imbalance is the root cause of poor performance as visualized in the Fig-2.

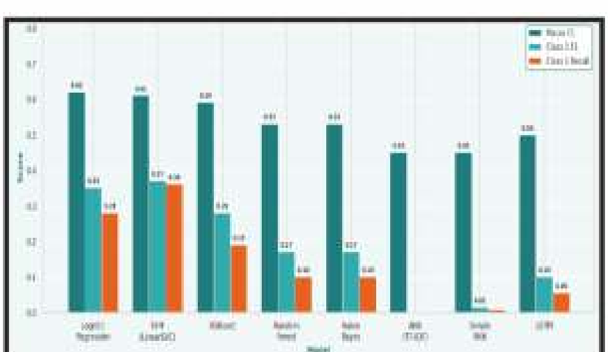

Fig 2. Baseline Model Performance without Imbalance Handling

C. Results after Imbalance Handling

Random Oversampling substantially improved minority class recall across all models is displayed in the Table 3. Logistic Regression (ROS) achieved a macro F1 of 0.64 and LSTM (ROS) reached 0.61. However, signs of overfitting on duplicate samples were observed in validation performance.

Table – 3. Random Over Sampling

Models	Macro F1	Recall
Logistic Regression	0.64	0.45
SVM	0.61	0.37
LSTM	0.61	0.53

Random Under sampling is presented in the table 4 found the further improved minority class recall (LSTM reached Class 1 Recall of 0.76) but caused under fitting for deep learning models due to reduced training data size.

Table – 4. Random Under Sampling

Models	Macro F1	Recall
Logistic Regression	0.61	0.70
XGBoost	0.62	0.68
LSTM	0.58	0.76

Class Weight Assignment produced the best results among non-BERT approaches is mentioned in the Table 5. Logistic Regression with class weight achieved a macro F1 of 0.64 and minority class recall of 0.49, training on the complete dataset without modifying data distribution

Table – 5. Using Class Weight

Models	Macro F1	Recall
Logistic Regression	0.64	0.49
XGBoost	0.63	0.48
LSTM	0.63	0.54

D. HateBERT Fine-Tuning and SMOTE and Class-Weight with BERT Embeddings.

It is observed that the best result is produced when BERT embeddings were combined with SMOTE and used to train downstream classifiers like SVM, XGBoost, and Random Forest. The highest overall macro F1 of 0.90 is achieved and shown in the Table 6.

The fine-tuned HateBERT model achieved the best performance of any standalone approach in this project. Table 7 presents the final evaluation results across all data splits. The comparison clearly shows a progressive improvement across all five phases, with the most dramatic jump occurring when HateBERT was introduced.

An inference test is conducted sample text which

Table – 6. Performance by Different Models

Model	Configuration	Macro F1	Class 1 Recall
Logistic Regression	TF-IDF + Class Weight	0.64	0.49
SVM	TF-IDF (Baseline)	0.61	0.36
Random Forest	TF-IDF + RUS	0.62	0.68
XGBoost	TF-IDF + RUS	0.62	0.67
LSTM	Word Embedding + Class Weight	0.63	0.54
HateBERT (Fine-tuned)	Class Weight	0.89	0.92
XGBoost + BERT	Class Weight	0.89	0.93
SVM + BERT	Class Weight	0.90	0.94
XGBoost + BERT + SMOTE	SMOTE	0.90	0.93
SVM + BERT + SMOTE	SMOTE	0.90	0.94

Table – 7. HateBERT Fine-Tuned Model

Split	Accuracy	Macro F1	Class 1 F1	Class 1 Recall
Training	98%	0.99	0.98	0.99
Validation	89%	0.89	0.88	0.94
Test	88%	0.89	0.87	0.92

output is presented in Fig-3. The sentence "I hate you so much for making me laugh this hard omg." and the line " yeah go ahead and block me, …" are correctly classified as NON-OFFENSIVE and OFFENSIVE respectedly by HateBERT model. This demonstrates the context-aware classification beyond simple ke

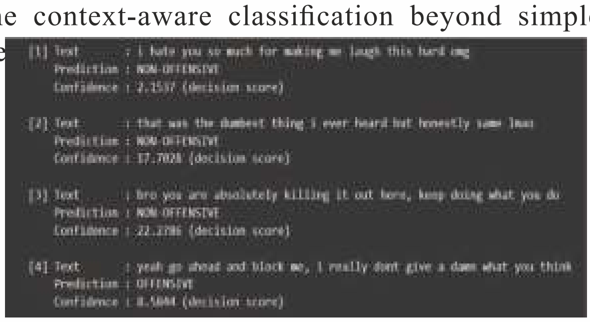

Fig 3. Output of Inference Test

V. Conclusions

This paper presents an ML-aided moderation system for detecting offensive comments on social me-dia. The project used the Tweets Dataset for Detection of Offensive Comments and implemented nine models ranging from traditional machine learning to transformer-based approaches. The central challenge of class imbalance, where non-offensive samples far outnumber offensive samples, caused many models to fail completely at the baseline stage, with the ANN predicting zero offensive samples.

Among traditional approaches, Logistic Regression with Class Weight performed the best with a macro F1 of 0.64. The most significant improvement came from fine-tuning HateBERT, which achieved a test macro F1 of 0.89 and a minority class recall of 0.92. When BERT embeddings were combined with SMOTE and used to train classifiers such as SVM, XGBoost, and Random Forest, the macro F1 reached 0.90 - the highest result in the project. The study clearly demonstrates that class imbalance must be addressed directly, and that transformer-based models such as HateBERT are far more effective than traditional approaches for detecting offensive comments in social media.

References

[1] S. Sadiq, A. Mehmood, S. Ullah, M. Ahmad, G. S. Choi, and B. W. On, "Aggression detection through deep neu-ral model on Twitter," Future Generation Computer Systems, vol. 114, pp. 120–129, 2021.

[2] T. Davidson, D. Warmsley, M. Macy, and I. Weber, "Automated hate speech detection and the problem of offensive language," in Proc. AAAI International Conference on Web and Social Media, vol. 11, no. 1, pp. 512–515, 2017.

[3] A. M. U. D. Khanday, S. T. Rabani, Q. R. Khan, and S. H. Malik, "Detecting Twitter hate speech in COVID-19 era using machine learning and ensemble learning tech-niques," International Journal of Information Management Data Insights, vol. 2, no. 2, Article 100120,2022.

[4] Á. MacDermott, M. Motylinski, F. Iqbal, K. Stamp, M. Hussain, and A. Marrington, "Using deep learning to de-tect social media trolls," Forensic Science International: Digital Investigation, vol. 43, 2022.

[5] T. Caselli, V. Basile, J. Mitrović, and M. Granitzer, "HateBERT: Retraining BERT for abusive language detection in English," in Proceedings of the Fifth Workshop on Online Abuse and Harms (WOAH), 2021.

[6] P. Fornacciari, M. Mordonini, A. Poggi, L. Sani and M. Tomaiuolo, A holistic system for troll detection on Twitter", Computers in Human Behavior, vol. 89, pp.

Satyajit Swain, Hrushikesh Behera,
Bishnu Das, Dr. Pulak Sahoo
Dept of CSE

Missile Woman of India

When people talk about powerful figures in science and defense, names from the West often dominate the conversation. But in India, one name quietly stands out, which is Dr. (Ms) Tessy Thomas, known as the “Missile Woman of India,” her journey is not just about rockets and technology but also about determination, resilience and breaking stereotypes.

Born in Alappuzha, Kerala, she grew up near a rocket launching station which sparked her curiosity about space and flight from a very young age. While many children dream of becoming doctors or teachers, she found herself fascinated by how things move in the sky. This early curiosity slowly shaped her career path.

She pursued engineering at Government Engineering College Thrissur and later specialized in guided missile technology. Her hard work eventually led her to join the Defence Research and Development Organisation (DRDO) where she became deeply involved in India's missile development programs.

What truly set Tessy Thomas apart was her leadership in the Agni missile program, one of India's most significant defense projects. She played a key role in the development of long-range ballistic missiles like Agni-IV and Agni-V. They represent India's growing strength in defense technology.

Being at the forefront of such a complex and high-pressure project is no small feat, especially in a field that has traditionally been dominated by men. But her story is not just about science. It is also about balance. While managing a demanding career, she also took care of her family life, something that is often overlooked when discussing successful professionals. Her journey shows that ambition and personal life don't always have to be at odds.

Over the years, she has received several awards and recognition for her contributions. She has become a role model for young women who want to step into fields like science, engineering and technology. She didn't just build missiles; she helped build confidence in a generation that now believes that no field is out of reach.

Sanigdha Samal
6th Sem, Dept. of EE

Performance Analysis of Predictive Maintenance Techniques using IoT Enabled Fiber Bragg Grating (FBG) Sensing Systems

The Industrial Revolution brought a revolutionary transformation in manufacturing by introducing mechanization and advanced machinery, significantly enhancing industrial productivity, efficiency, and large-scale production capabilities. The transition from manual labor to machine-based operations enabled industries to achieve greater precision and operational speed. However, the increasing dependence on machinery also introduced several technical challenges, among which machine vibration has become one of the most critical concerns in industrial systems. Vibrations are naturally generated during machine operations due to rotating and moving components, friction, imbalance, and mechanical interactions. Although a certain level of vibration is unavoidable and often considered acceptable, excessive or abnormal vibrations can negatively affect machine performance, reliability, and operational safety.

Uncontrolled machine vibrations can lead to severe consequences, including accelerated wear and tear of components such as bearings, shafts, gears, and couplings. Continuous exposure to excessive vibrations may result in structural fatigue, misalignment, loosened mechanical parts, and unexpected machine failures, leading to costly operational downtime and production losses. In precision manufacturing sectors, abnormal vibrations can also compromise product quality and reduce process accuracy. Moreover, excessive vibration contributes to higher energy consumption and increased maintenance requirements, affecting overall industrial efficiency and sustainability. These challenges emphasize the need for effective vibration monitoring and control to maintain equipment health and ensure uninterrupted industrial operations.

Machine vibration analysis has become an essential tool for condition monitoring and fault diagnosis, as vibration characteristics often reflect the health status of machinery. Early detection of vibration abnormalities enables the identification of faults such as imbalance, shaft misalignment, looseness, resonance, and bearing defects before they develop into major failures. In this regard, predictive maintenance has gained importance as a proactive maintenance strategy that continuously monitors equipment condition and predicts faults in advance. Unlike conventional maintenance methods based on scheduled servicing or reactive repair, predictive maintenance minimizes unexpected breakdowns, improves equipment lifespan, and reduces maintenance costs.

The efficiency of predictive maintenance depends largely on reliable sensing technologies used for vibration measurement. Conventional sensors, including accelerometers, displacement sensors, and piezoelectric devices, are widely employed for monitoring machine vibrations. However, recent technological advancements have highlighted the advantages of Fiber Bragg Grating (FBG) sensors, which offer high sensitivity, immunity to electromagnetic interference, durability, and the ability to provide real-time monitoring in harsh industrial environments. FBG sensors are capable of detecting minute changes in vibration and strain, making them highly suitable for machine condition monitoring.

Additionally, integrating FBG sensors with advanced fault detection techniques, signal processing methods such as Fast Fourier Transformation (FFT), and intelligent Decision Support Systems (DSS) has improved fault diagnosis accuracy. These technologies enable efficient vibration signal analysis, accurate fault classification, informed maintenance decisions, and improved operational performance while reducing maintenance costs and enhancing industrial safety.

Dr. Deepak Ranjan Nayak
Dept. of EEE

From DNA to Deep Space: The Convergence of Bioinformatics, Artificial Intelligence, and Space Technology

Abstract

The convergence of bioinformatics, artificial intelligence (AI), and space technology is transforming modern science. Bioinformatics enables the analysis of complex biological data, AI accelerates genomic interpretation and disease prediction, and space technology provides unique environments for studying life under extreme conditions. Together, these fields are advancing precision medicine, space medicine, and autonomous scientific research, creating new opportunities for healthcare and long-duration space exploration.

Keywords

Bioinformatics, AI, Space Technology, Genomics, Multi-omics

Introduction

Bioinformatics and space technology are rapidly advancing scientific fields. The discovery of DNA as the genetic material by Avery, MacLeod, and McCarty, Hershey and Chase, and the DNA double-helix model by Watson and Crick laid the foundation for modern genomics. Space exploration has enabled the study of biological systems under microgravity and radiation, while AI helps analyze these complex datasets to better understand cellular responses and improve human health.

Artificial Intelligence in Genomic and Biomedical Research

The rapid growth of genomic, transcriptomic, and proteomic data has made AI an indispensable tool in bioinformatics. Machine learning algorithms identify disease-associated genetic variations, improve next-generation sequencing analysis, and detect potential therapeutic targets with greater speed and accuracy.

AI also drives precision medicine by integrating genomic, clinical, and environmental data to predict disease susceptibility, treatment response, and patient outcomes. These capabilities support earlier diagnosis and personalized healthcare strategies, shifting medicine from reactive treatment to proactive prevention.

Spaceflight Multi-omics and Systems Biology

Spaceflight multi-omics integrates genomics, transcriptomics, proteomics, metabolomics, and epigenomics to understand how living systems adapt to space environments. Studies have shown that prolonged exposure to microgravity and radiation affects mitochondrial function, immune responses, metabolism, and oxidative stress. Fig. 1[1] describes the use of multiple omics technologies to study life in a concerted way.

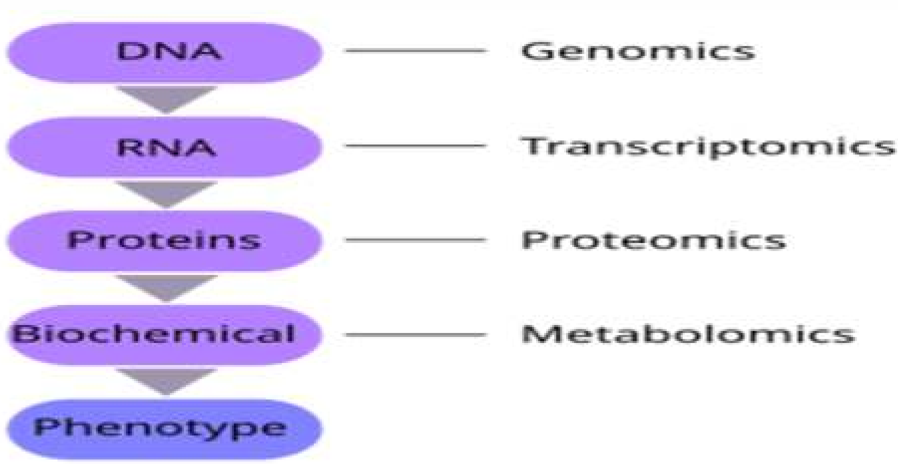

Fig. 1: Multiomics integrates diverse omics data for systems biology

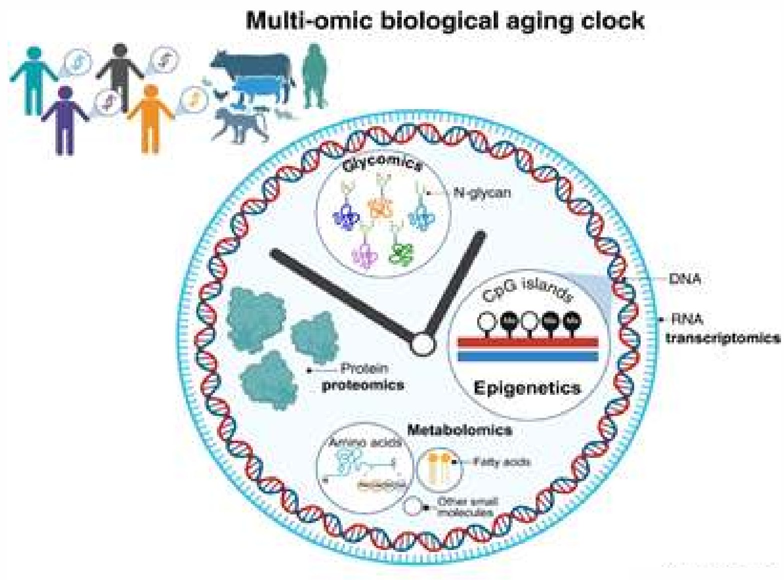

Fig. 2 Epigenetic Aging Biomarkers

AI-based analysis of multi-omics data uncovers molecular pathways and predicts biological outcomes, providing valuable insights for protecting astronaut health during future missions to the Moon, Mars, and beyond.

Epigenetic Clocks and Predictive Healthcare

Epigenetics investigates changes in gene expression without altering DNA sequences. DNA methylation patterns serve as biomarkers for biological aging and disease risk. AI-powered bioinformatics tools analyze these patterns to predict conditions such as cancer, cardiovascular disease, and neurodegenerative disorders. Fig. 2 [2] presents a multi-omic aging clock for biological age estimation and biomarker discovery.

Spaceflight can also influence epigenetic regulation, making epigenetic clocks valuable for monitoring astronaut health and understanding the long-term biological effects of space travel.

Automated and Self-Driving Laboratories

Automated and Self-Driving Laboratories (SDLs) combine AI, robotics, and automation to conduct scientific experiments with minimal human intervention. These systems can design experiments, analyze results, and refine future investigations using machine learning.

SDLs are especially valuable for deep-space missions, where communication delays and limited crew availability require autonomous scientific operations. They also have broad applications in biotechnology, pharmaceuticals, and materials science.

Future Perspectives and Challenges

Despite remarkable progress, challenges remain, including limited spaceflight biological datasets, data integration, computational complexity, and ethical concerns regarding genomic information. Future research should emphasize explainable AI, standardized databases, secure data-sharing frameworks, and emerging technologies such as quantum computing and digital twins.

Conclusion

The convergence of bioinformatics, AI, and space technology is redefining biological research and space exploration. AI-driven genomics, spaceflight multi-omics, epigenetic analysis, and autonomous laboratories are improving healthcare while supporting sustainable human exploration beyond Earth. As these technologies continue to evolve, they will play a vital role in future scientific discoveries and long-duration space missions.

Resources :

[1] J. Kim et al., "Single-cell multi-ome and immune profiles of the Inspiration4 crew," Nature Communications, vol. 15, 2024.

[2] S. Wu et al., "Toward equitable biomarkers of aging: Rethinking methylation clocks," Trends in Genetics, 2025.

Nancy Suman
4th Sem, Dept. of ECE

Ocean Acidification

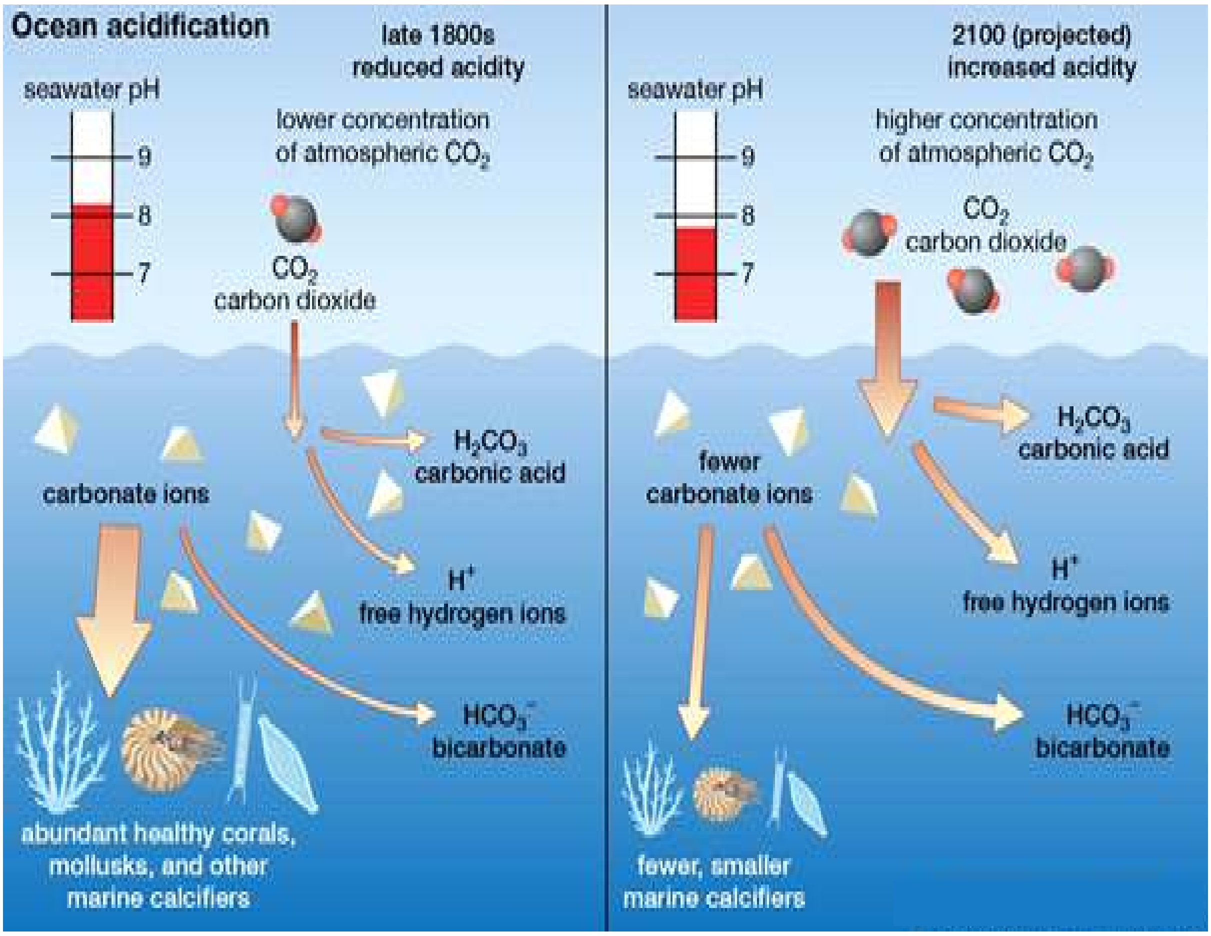

Global temperature rise has not only affected the surface, but it is also the main cause of ocean acidification. Our oceans absorb about 30% of the carbon dioxide that is released into the Earth's atmosphere. As higher concentrations of carbon emissions are released due to human activities such as burning fossil fuels, as well as effects of global climate change, such as increased rates of wildfires and this can lead to an increased amount of carbon dioxide that is absorbed back into the sea. The smallest change in the acidity scale can have a significant impact on the acidity of the ocean. Ocean acidification has devastating impacts on marine ecosystems and species, its food webs, and provoke irreversible changes in habitat quality. Once acidity (pH) levels reach too low, marine organisms such as oysters, their shells, and skeletons could even start to dissolve.

However, one of the biggest environmental problems from ocean acidification is coral bleaching and subsequent coral reef loss. This phenomenon occurs when rising ocean temperatures disrupt the symbiotic relationship between the reefs and algae that lives within it, driving away the algae and causing coral reefs to lose their natural vibrant colours. Some scientists have estimated that coral reefs are at risk of being completely wiped out by 2050. Higher acidity in the ocean would obstruct coral reef systems' ability to rebuild their exoskeletons and recover from these coral bleaching events.

Source: [*https://earth.org/the-biggest-environmental-problems-of-our-lifetime/*](https://earth.org/the-biggest-environmental-problems-of-our-lifetime/)

www.britannica.com

Text-Independent Speaker Recognition under Clean & Multi-Noise Conditions: A Unified Evaluation of Acoustic Feature Extraction & Machine Learning Classifiers

Abstract *– Automatic speaker recognition systems must per-form reliably across both controlled and real-world acoustic environments. This paper presents a unified evaluation of three acoustic feature extraction techniques — Mel Frequency Cepstral Coefficients (MFCC), Linear Predictive Coding (LPC), and Gammatone Frequency Cepstral Coefficients (GFCC) — along with a combined feature fusion strategy, assessed under both clean and multi-noise-augmented conditions on a 50-speaker subset of the LibriSpeech corpus. Six classifiers are evaluated: Support Vector Machine (SVM), Decision Tree (DT), Random Forest (RF), Extra Trees (ET), Voting Classifier, and Convolutional Neural Network (CNN). Under clean conditions, combined feature fusion with SVM achieves 97.13% accuracy (F1: 0.971). Under a unified multi-noise scheme combining white noise, babble noise, and ambient noise at SNR = 10 dB, the same configuration retains 88.96%. Among individual features, GFCC demonstrates superior noise robustness (SVM: 78.70%) over MFCC (SVM: 76.43%), while MFCC leads under clean conditions (ET: 92.87%). CNN uniquely maintains 89.12% accuracy across all conditions owing to its spectrogram-based representation being independent of the hand-crafted feature pipeline. These findings provide actionable deployment guidance for speaker recognition systems across diverse acoustic environments.*

Keywords *– speaker recognition, MFCC, LPC, feature fusion, noise robustness, ensemble learning*

I. Introduction

Voice-based biometric authentication has seen rapid growth driven by the proliferation of smart devices, virtual assistants, and call-centre automation [1]. Speaker recognition is attractive for its non-intrusive nature and low hardware requirements [2]. Practical deployments rarely operate under clean acoustic conditions — white Gaussian noise, babble interference, and ambient environmental sounds cause significant accuracy degradation [3]. The choice of acoustic feature representation is the primary factor governing both clean-condition accuracy and real-world noise robustness. MFCC has dominated speaker recognition owing to its mel-scale auditory alignment [4].

LPC captures vocal tract characteristics but is sensitive to additive noise [5, 6]. GFCC, based on the gammatone auditory filterbank with cubic-root amplitude compression, was designed specifically for noise-robust conditions [7]. Feature fusion strategies combining multiple representations have consistently outperformed individual features by exploiting complementary information [8, 9].

Despite this body of work, a controlled simultaneous comparison of all three feature types under a unified multi-noise augmentation scheme across a representative classifier set remains limited. This paper addresses that gap with the following contributions:

1) A unified evaluation of four feature strategies (MFCC, LPC, GFCC, and combined fusion) across six classifiers under identical clean and multi-noise experimental conditions on 50 speakers.
2) A novel multi-noise augmentation scheme combining white noise, babble noise, and ambient background noise at SNR = 10 dB, providing a more realistic noise characterisation than single-noise evaluations.
3) A dedicated clean-to-noisy degradation analysis per feature type and classifier, producing practical deployment recommendations for diverse acoustic environments.

II. System Overview

A. Dataset and Preprocessing

All experiments were conducted on 50 speakers drawn from the LibriSpeech train-clean-100 partition [10], yielding approximately 5,500 audio utterances in .flac format. Audio was resampled to 16 kHz and each utterance was clipped to a fixed duration of 3s. Amplitude normalisation is shown in equation (1):

$$X_{norm}(n) = \frac{X(n)}{\max(|X(n)|)} \quad (1)$$

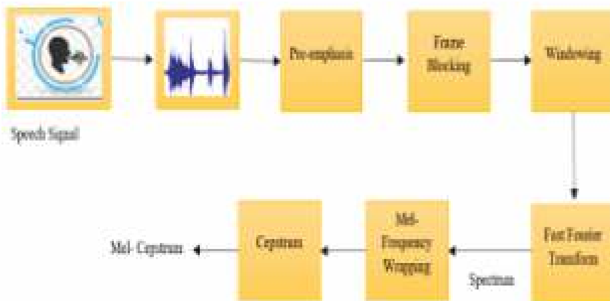

Fig. 1. MFCC feature extraction pipeline: pre-emphasis, frame blocking, windowing, FFT, mel-frequency wrapping, and cepstral extraction via DCT.

The dataset was partitioned into 80% training and 20% testing subsets using stratified random sampling to ensure balanced speaker representation in both splits.

B. Noise Augmentation

To simulate realistic joint noise conditions, a unified multi-noise augmentation scheme was employed. Three noise sources were combined into a single mixed noise signal which is shown in equation (2):

$$n(t) = \frac{n_w(t) + n_b(t) + n_{bg}(t)}{3} \quad (2)$$

where n_w is white Gaussian noise, n_b is babble noise (multi-talker overlapping speech), and n_{bg} is background ambient noise sourced from the ESC-50 environmental sound corpus. The mixed noise signal was added to clean recordings via SNR-controlled scaling described in equation (3):

$$x'(n) = x(n) + \propto \cdot\, n(n) \quad (3)$$

where α is set to achieve SNR = 10 dB. This design tests the intrinsic noise immunity of each feature extractor under a genuine joint noise condition, providing a more realistic characterisation than single-noise evaluations.

C. Feature Extraction

MFCC (Fig. 1): Pre-emphasis with coefficient 0.97 is applied, followed by 25 ms Hamming-windowed frames with 10 ms shift. The magnitude spectrum is mapped onto a 40-channel mel filterbank via equation (4)

$$Mel(f) = 2595 log_{10}^{1} + \frac{f}{100} \quad (4)$$

followed by log compression and DCT to yield 13 cepstralcoefficients per frame. Delta (Δ) and delta-delta (Δ^2) temporal derivative features are appended to produce 39 coefficients per frame. Mean and standard deviation aggregation over all frames yields a 78-dimensional utterance-level feature vector.

LPC: LPC is defined in Equation (5), where the speech signal is modelled as an all-pole vocal tract filter of order p = 16:

$$X(n) = \sum_{k=1}^{p} a_k x(n-k) + e(n) \quad (5)$$

where a_k are predictor coefficients estimated via Levinson-Durbin recursion and *e(n)* is the prediction residual. Mean and standard deviation aggregation over frames yields the utterance-level vector.

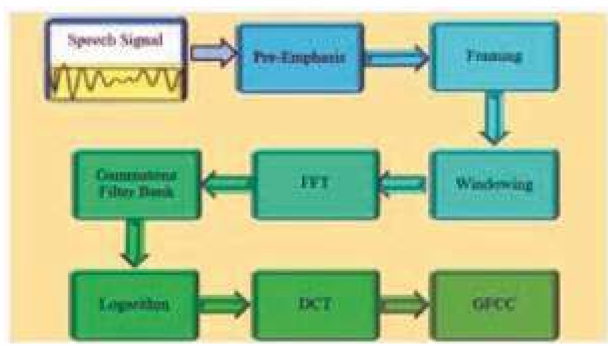

Fig.-2. GFCC feature extraction pipeline: pre-emphasis, framing, windowing, FFT, gammatone filterbank, logarithm, and DCT.

GFCC (Fig. 2): A 64-channel gammatone filterbank span-ning 50–8000 Hz on the Equivalent Rectangular Bandwidth (ERB) scale models basilar membrane frequency selectivity. The impulse response of a gammatone filter centred at frequency f_c is shown in Equation (6):

$$g(t) = t^{n-1} e^{-2\pi bt} \cos(2\pi f_c t) \quad (6)$$

where *n* is the filter order and b is the ERB-related bandwidth parameter. Cubic-root amplitude compression is calculated using Equation (7):

$$E_{comp} = E^{1/3} \quad (7)$$

It simulates cochlear non-linearity and constrains the dynamic range of channel outputs, providing inherent noise resistance [8]. DCT is applied to yield 20 cepstral coefficients per frame, similarly aggregated to a fixed-dimensional utterance vector.

Combined Fusion: The three feature vectors are concate-nated to form a unified representation as shown in Equation (8):

$$F_{combined} = [F_{MFCC} \| F_{LPC} \| F_{GFCC}] \tag{8}$$

This late-feature fusion preserves spectral (MFCC), source-filter (LPC), and auditory (GFCC) information independently, allowing classifiers to exploit complementary speaker characteristics [9]. All feature vectors are z-score normalised prior to classification.

D. Classification Models

Six models were evaluated across all feature types and conditions. SVM with RBF kernel (C and γ tuned via 5-fold cross-validated grid search, $C \in \{0.1, 1, 10, 100\}$). Decision Tree (DT) with Gini impurity criterion and cross-validated maximum depth. Random Forest (RF) and Extra Trees (ET) with 100 estimators each; ET introduces additional split-level randomisation for variance reduction. Voting Classifier using soft probability-weighted voting is calculated using Equation (9).

$$y^{\wedge} = argmax \sum_{k=1}^{K} w_k P_k \left(y = i|x\right) \tag{9}$$

Table–1. Accuracy (%) and F1 Score Under Clean Conditions (50 Speakers)

Model	**MFCC**		**LCC**		**GFCC**		**Combined**	
	Acc	F1	Acc	F1	Acc	F1	Acc	F1
SVM	91.22	0.911	57.30	0.570	85.13	0.853	**97.13**	**0.971**
RF	91.22	0.911	54.43	0.536	74.09	0.740	94.70	0.946
ET	92.87	0.928	55.83	0.544	75.13	0.748	94.87	0.948
DT	64.43	0.647	31.04	0.311	45.83	0.460	65.83	0.661
Voting	89.30	0.892	40.26	0.400	64.70	0.641	89.83	0.896
CNN	89.12	0.890	89.12	0.890	89.12	0.890	89.12	0.890

where P_k is the posterior probability from the *k-th* base estimator and w_k is its weight. CNN with two Conv2D layers (32 and 64 filters, 3×3 kernels, ReLU activation), Batch Normalisation, Max Pooling, Dropout (0.3), Global Average Pooling, and Softmax output over 50 speaker classes, trained on 128×128 MFCC spectrograms using the Adam optimiser (lr = 0.001) with early stopping (patience = 10). All implementations used scikit-learn and TensorFlow.

III. Results and Discussion

A. Clean Condition Performance

Table I presents accuracy and F1 scores under clean conditions across all feature types and classifiers. Combined feature fusion with SVM achieves the highest accuracy of 97.13% (F1: 0.971), confirming that spectral (MFCC), source-filter (LPC), and auditory (GFCC) representations provide complementary discriminative information. The SVM gain of +5.91 pp over MFCC alone reflects the richer, more separable feature space constructed by the RBF kernel operating on the fused high-dimensional vector [11].

Among individual features, MFCC leads with ET at 92.87% (F1: 0.928), consistent with the mel-scale filterbank's well-established perceptual alignment with human auditory process-ing [4]. GFCC with SVM achieves 85.13%, occupying an intermediate position and confirming strong representational capacity under clean speech despite being primarily designed for noise-robust conditions [7]. LPC consistently underperforms (SVM: 57.30%, DT: 31.04%) due to the fundamental limitations of the all-pole vocal tract model in capturing anti-resonances in nasal and fricative speech [6]. CNN achieves a uniform 89.12% regardless of input feature type, as its spectrogram-based 2D representation is independent of the hand-crafted feature pipeline [12].

B. Performance Under Multi-Noise Augmentation

Table - II Accuracy (%) and F1 score under Multi-Noise (SNR = 10 Db)

Model	MFCC		LPC		GFCC		Combined	
	Acc	F1	Acc	F1	Acc	F1	Acc	F1
SVM	76.43	0.764	64.87	0.645	78.70	0.788	**88.96**	**0.889**
RF	71.04	0.709	58.17	0.578	63.39	0.629	82.52	0.824
ET	75.13	0.749	59.13	0.580	67.04	0.664	83.04	0.829
DT	43.30	0.433	31.04	0.313	39.48	0.396	47.30	0.474
Voting	62.26	0.619	45.13	0.448	54.43	0.538	70.61	0.701
CNN	89.12	0.890	89.12	0.890	89.12	0.890	89.12	0.890

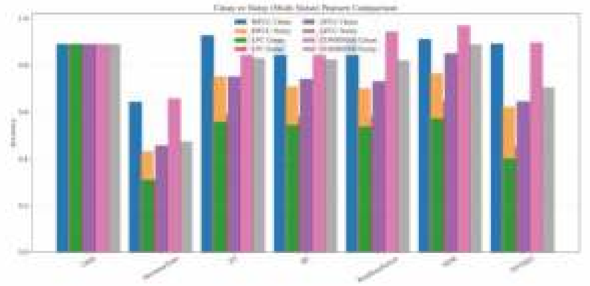

Fig. 3. Clean vs. multi-noise accuracy comparison across all feature types and classifiers, illustrating the degradation profile under joint noise augmentation at SNR = 10 dB

Table II presents results under multi-noise augmentation at SNR = 10 dB. Combined fusion with SVM retains 88.96% (F1: 0.889), the strongest noise-robust result among all classical configurations. GFCC demonstrates superior individual noise robustness with SVM at 78.70%, outperforming MFCC at 76.43%, validating the gammatone filterbank's noise-resistance properties through cubic-root compression and ERB-scale channel spacing [7], [8]. LPC exhibits an anomalous behaviour under noise: SVM accuracy increases from 57.30% (clean) to 64.87% (noisy). This counter-intuitive result is attributable to LPC's already-constrained modelling capacity — its all-pole assumptions introduce a performance ceiling that moderate additive noise cannot degrade further [6]. CNN uniquely maintains 89.12% across all noise conditions, confirming the robustness of spectrogram-based 2D representations to additive noise [13].

C. Clean-to-Noisy Degradation Analysis

Fig. 3 illustrates the accuracy degradation profile across all feature types and classifiers under the transition from clean to multi-noise conditions. MFCC suffers the largest degradation among individual features (ET: −17.74 pp; SVM: −14.79 pp), consistent with the mel filterbank's sensitivity to spectral distortion introduced by additive noise. GFCC degrades more moderately (ET: −8.09 pp; SVM: −6.43 pp), demonstrating the noise-resistance benefit of cubic-root compression and biologically inspired ERB-scale channel spacing [8]. Combined fusion degrades by −8.17 pp with SVM (97.13% → 88.96%), which, while non-trivial in absolute terms, still represents thebest absolute accuracy under noise among all configurations. Decision Tree and Voting degrade severely under noise across all features, confirming their instability in high-dimensional, noise-corrupted feature spaces.

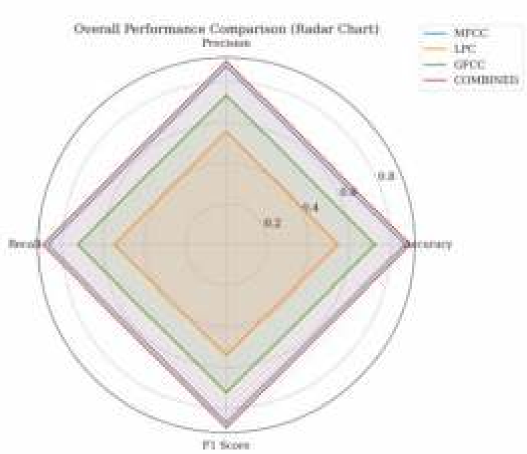

Fig. 4. Performance radar chart: MFCC, LPC, GFCC, and Combined across Accuracy, Precision, Recall, and F1 (clean conditions).

D. ROC-AUC and Deployment Recommendations

Under clean conditions, all features achieve ROC-AUC ≈ 1.00 with SVM, ET, and CNN. Under multi-noise, AUC degrades substantially: MFCC = 0.58, LPC = 0.73, GFCC = 0.56, Combined = 0.60. LPC's higher noise-AUC (0.73) despite the lowest accuracy suggests its autocorrelation features retain ranking structure under noise — relevant for threshold-based verification [2]. Fig. 4 confirms combined features dominate all four metric axes; MFCC and GFCC are closely competitive; LPC trails.

For clean environments, combined fusion with SVM (97.13%) is optimal. For noisy environments (SNR ≈ 10 dB), the same combination retains 88.96%; among individual features, GFCC-SVM (78.70%) outperforms MFCC-SVM (76.43%). For unknown noise conditions, CNN (89.12% uniform) is the most reliable choice.

IV. Conclusion

This paper presents a unified evaluation of text-independent speaker recognition across clean and multi-noise-augmented conditions using MFCC, LPC, GFCC, and combined feature fusion against six classifiers on a 50-speaker LibriSpeech subset. Combined fusion with SVM achieves 97.13% under clean conditions and retains 88.96% under multi-noise at SNR = 10 dB. Among individual features, MFCC leads under clean conditions (ET: 92.87%) while GFCC demonstrates superior noise robustness (SVM: 78.70%). CNN uniquely maintains 89.12% across all conditions, making it the pre-ferred choice for unpredictable noise environments. ROC-AUC analysis reveals substantial degradation under noise with important implications for verification threshold design. Future work will investigate noise-aware training at variable SNRs, transformer-based embeddings (ECAPA-TDNN, WavLM), and adversarial domain adaptation for cross-environment robustness.

References

[1] D. A. Reynolds, “Speaker identification and verification using Gaussian mixture models,” Speech Commun., vol. 17, no. 1–2, pp. 91–108, 1995.

[2] T. Kinnunen and H. Li, “An overview of text-independent speaker recognition: from features to supervectors,” Speech Commun., vol. 52, no. 1, pp. 12–40, 2010.

[3] Z. Zhang, Y. Zhao, and D. Wang, “A survey of speaker

recognition: fundamental theories, recognition methods and opportunities," IEEE Access, vol. 10, pp. 99059–99081, 2022.

[4] S. B. Davis and P. Mermelstein, "Comparison of parametric repre-sentations for monosyllabic word recognition in continuously spoken sentences," IEEE Trans. Acoust., Speech, Signal Process., vol. 28, no. 4, pp. 357–366, 1980.

[5] B. S. Atal and S. L. Hanauer, "Speech analysis and synthesis by linear prediction of the speech wave," J. Acoust. Soc. Am., vol. 50, no. 2B, pp. 637–655, 1971.

[6] J. Makhoul, "Linear prediction: a tutorial review," Proc. IEEE, vol. 63, no. 4, pp. 561–580, 1975.

[7] Y. Shao, Z. Jin, D. Wang, and S. Srinivasan, "An auditory-based feature for robust speech recognition," in Proc. ICASSP, 2009, pp. 4625–4628.

[8] X. Valero and F. Alias, "Gammatone cepstral coefficients: biologically inspired features for non-speech audio classification," IEEE Trans. Multimedia, vol. 14, no. 6, pp. 1684–1689, 2012.

[9] R. Jahangir et al., "Speaker identification through artificial intelligence techniques: a comprehensive review," Expert Syst. Appl., vol. 171, p. 114591, 2021.

[10] T. Zhou, L. Chen, and R. Tao, "Ensemble feature learning for noise-robust speaker identification using gammatone and mel-frequency cepstral representations," Digit. Signal Process., vol. 148, p. 104435, 2024.

[11] W. M. Campbell, D. E. Sturim, and D. A. Reynolds, "Support vector machines using GMM supervectors for speaker verification," IEEE Signal Process. Lett., vol. 13, no. 5, pp. 308–311, 2006.

[12] Z. Bai and X.-L. Zhang, "Speaker recognition based on deep learning: an overview," Neural Networks, vol. 140, pp. 65–99, 2021.

[13] V. Panayotov, G. Chen, D. Povey, and S. Khudanpur, "LibriSpeech: an ASR corpus based on public domain audio books," in Proc. ICASSP, 2015, pp. 5206–5210.

Abinash Dash, **Pritish Kumar Lenka,**
Sutikhna Behera, Pratham Tripathy
Dept. of ECE

Brain Training Gaming Technology, Enables Fast BCI Training for Medical Use

Researchers at Yale University have developed a new brain-computer interface (BCI) that allows people to play video games using only their brain activity. By using real-time fMRI (functional MRI), the team demonstrated that users can control a computer efficiently through their thoughts alone. The findings were published in Nature Neuroscience. The study revealed that brain activity follows established neural pathways. Researchers found that learning to use a BCI becomes much easier when the system is designed to work with those existing pathways rather than against them. When a BCI aligns with the brain's natural organization, users gain control quickly, and their brain activity adapts to support learning. Systems that do not match this structure produce little or no improvement.

Source: https://scitechdaily.com/

The Fabric of the Universe - Stars or Galaxies?

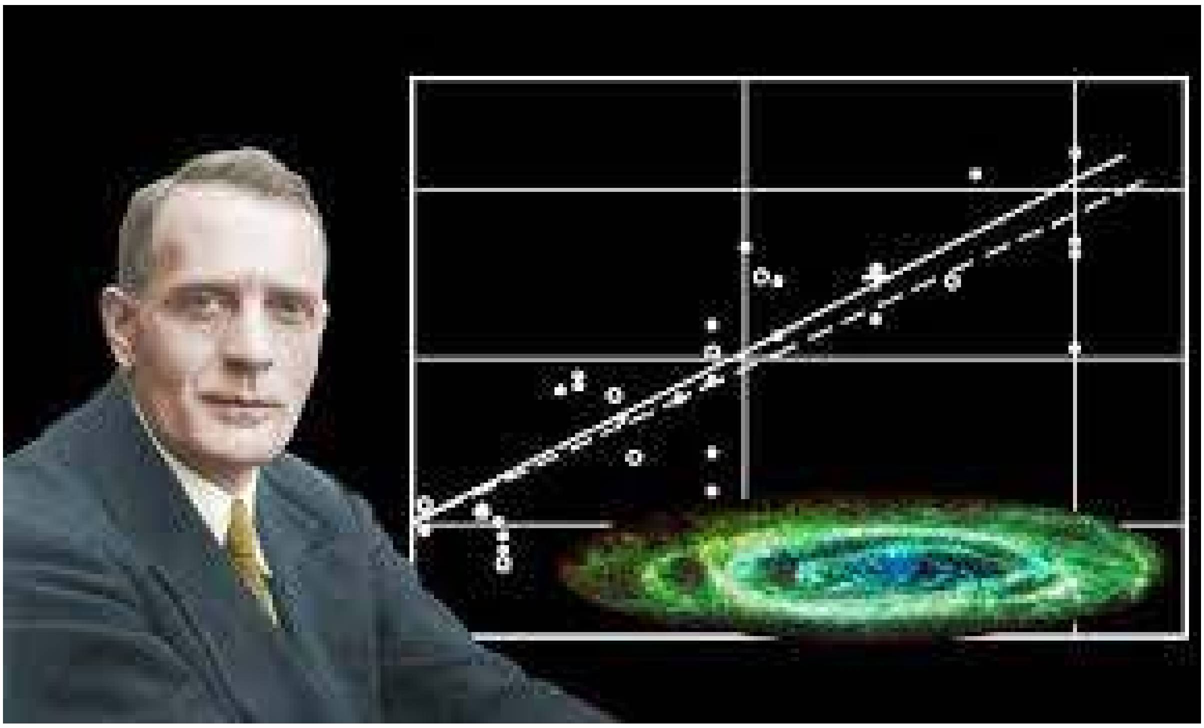

Edwin Hubble was an American astronomer, who proved that galaxies are the fundamental building blocks, or "fabric" of the universe. The accepted notion till the early 1900s was that the billions of stars in the Milky Way galaxy constituted the universe, and there was nothing beyond that. That perspective changed dramatically, after a young man named Edwin Hubble used the 100-inch Hooker Telescope at Mount Wilson Observatory in California to study what was then known as the Andromeda Nebula; this object has appeared as an elongated cloud of light for centuries.

He made the key discovery in 1923, which he called the "Island Universe" Hypothesis. Hubble postulated that he was able to resolve individual stars in this "nebula." By identifying some cepheid variable stars in the Andromeda Nebula, Hubble calculated its distance, placing it millions of light-years away, far beyond the known limits of the Milky Way. Cepheid variable stars are yellow supergiant stars that pulsate radially, brighten and dim, in a rhythmic fashion. Moreover, as their pulsation period is directly related to their intrinsic luminosity (brightness), it allows astronomers to use them as "standard candles" to measure distances to distant galaxies. Hubble proved that many objects previously thought to be clouds of dust and gas and classified as "nebulae" were actually galaxies beyond the Milky Way.

Another major finding followed in 1929. Hubble discovered that all galaxies are moving away from us, with their recessional velocity increasing in proportion to their distance from Earth, demonstrating that the universe is expanding. The further the galaxies are from us, the faster they are moving away - now called 'Hubble's Law'. All galaxies appear to be red-shifted from any point in the universe.

And finally, Hubble devised a system for classifying galaxies by their structure - elliptical, spiral, barred spiral, lenticular and irregular, a convention which is still adopted today.

Hats off to Edwin Hubble for his truly stellar performance!

Content excerpted from Wikipedia and other web sources

Dr. Jaideep Talukdar
Dept. of BSH

Publication Cell
Tel: 9937289499/8260333609
Email: publication@silicon.ac.in

www.silicon.ac.in

The Science & Technology Magazine

Digital Digest

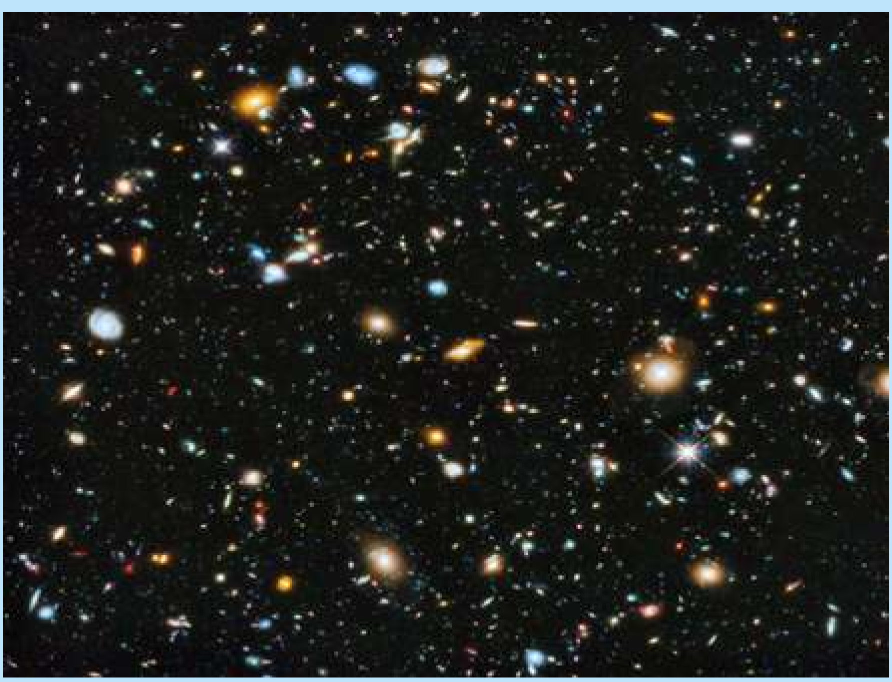

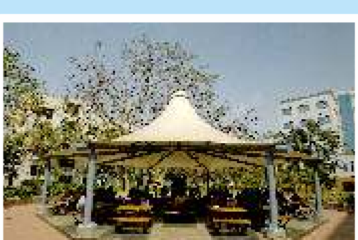

Silicon University, Odisha

Contents